Development of a Drone-based Ground Penetrating Radar System for Astrophysics Research

Michael Hétu

Supervised by Prof. Cynthia Chiang

Departement of Physics, McGill University

April 18, 2024

Abstract

This thesis explores the development of a drone-based ground penetrating radar (GPR) system using a software-defined radio (SDR). The project aims to address the challenges involved in producing accurate soil analysis for beam response mapping of radio antennas conducting cosmological astronomy surveys at low frequencies. The GPR system utilizes the frequency modulated continuous wave (FMCW) technique with a linear frequency modulated (LFM) chirp, implemented on the Ettus B210 SDR. The report details the methodology, including the synthetic wideband waveform (SWW) reconstruction algorithm, communication protocol with the SDR, and presents results demonstrating the system's capability to achieve high resolution and accuracy in both a loopback test and a test involving the detection of a highly reflective metallic surface. Future steps involve implementing amplification and improving the speed of both scanning and post-processing. The findings suggest that the SWW algorithm provides a viable alternative to commercial GPR systems, overcoming hardware limitations and offering flexibility for various applications, including astrophysics and cryospheric research.

1 Introduction

Neutral hydrogen, the most abundant element in the universe, has long been an important part of cosmology, serving as an invaluable tracer for understanding the universe's history thanks to its characteristic 21cm emission line. Measuring this signal redshifted to low frequencies, below 200 MHz, allows cosmologists to probe the early periods in the universe's

history that remain unobserved. Projects such as the Mapper of IGM Spin Temperature (MIST) are attempting to shed light on this era by measuring the average sky brightness of the 21cm signal. MIST is composed of a horizontal blade dipole antenna supported 52cm off the ground by a fiberglass structure. The structure is placed directly on the ground, without a metallic ground plane [1]. Conducting radio astronomy surveys at such low frequencies introduces numerous systematic errors due to human and astronomical factors, pushing experiments like these into remote locations, such as the McGill Arctic Research Station (MARS) on Axel Heiberg Island in northern Nunavut. Careful attention must be paid to the proper calibration of radio antennas, including their spatial response on the sky, or the "beam pattern." Since MIST does not use a reflective ground plane, the incoming EM waves are not being propagated back into the antenna, but are instead interacting with the soil, resulting in an overall ground loss affecting the beam pattern and the measured sky temperature. In order to account for this loss, a complete understanding of the different soil layers and their dielectric properties, notably their conductivity and relative permittivity, are required to accurately model these interactions [2]. We can obtain this information using ground penetrating radar. This chapter describes the functioning of Ground Penetrating Radar and the limitations of commercial systems that led to the development of a GPR system of our own.

1.1 Ground Penetrating Radar

Ground penetrating radar is a non-invasive remote sensing method that allows for the analysis and mapping of subsurface structures. It works by first sending electromagnetic (EM) waves into the soil via an antenna. The EM waves interact with the soil in well-defined ways, reflecting off objects, structures large and small, and at the boundary between soil layers, producing a very information-dense reflected signal due to the highly structured and anisotropic composition of soil. These reflections are recorded by an antenna. Following signal filtering and processing, we are left with a single 1-dimensional 'A-scan', showing the different reflections and their intensities throughout the scan, known as a range profile. Joining multiple A-scans together produces a 'B-scan', showing a 2-dimensional slice of the subsurface. Joining these together gives us a 3-dimensional 'C-scan'. The scope of this thesis is confined to the 1-D A-scan [3].

This technology is commonly used in civil engineering, geographic surveys, and geological studies among others. Ice penetrating radar (IPR), a subset of GPR, is employed by cryospheric researchers to study ice shelves and glaciers. While GPR is typically operated in the GHz range, IPR sticks to the very low MHz range, on the order of 100-200 MHz, due to the higher absorption of water at higher frequencies [4]. Since radio-astronomy projects

such as MIST are fortuitously located in the high Arctic where cryospheric research also takes place, the shared need for GPR produces the perfect conditions for interdisciplinary collaboration.

Of particular interest to us, and to some glaciology research, is the ability to measure the electric properties of soil. While typical GPR subsurface mapping requires a prior knowledge of the speed of light in the soil, c, to convert a time-of-flight measurement of a reflection to a feature depth map, our use case instead requires that we extract this information from the range profile. Common mid-point scanning is a method of measuring c, whereby the transmit and receive antennas are increasingly spaced apart, allowing us to determine the speed of light through the medium by analyzing the slope of the hyperbola reflection from a buried object or layer interface [5]. From the slope, soil electric properties can be inferred.

1.2 Time Domain vs. Frequency Domain

While there are a large number of different methods and algorithms to produce GPR scans, they are usually cast in one of two categories; time domain or frequency domain. Within the time domain systems, the most common variety is pulse radar, in which a very short and powerful EM pulse is transmitted, usually a Gaussian pulse or one of its derivatives with a duration τ on the order of nanoseconds or less. Following the emission of the pulse, there is a dwell time, during which the reflections of the pulse in the soil are recorded and their time of flight (TOF) directly plotted, hence the name. The performance of any radar system is characterized by its maximum range R_{max} and its range resolution ΔR. In time domain radar, the former is mostly dependant on the dwell time between pulses, while the latter is the minimal time between two reflections such that the reflected pulses can be resolved [3], and is typically described by the formula

$$\Delta R = \frac{\tau c}{2}. \tag{1}$$

While the simplest of GPR systems, there are some downsides. Electronics capable of producing such short pulses are often complex and require large amounts of energy [3], and the analog to digital converter (ADC) is required to sample the incoming signals at a high enough rate to not further limit the range resolution, adding on computational complexities for handling and storing the high bitrate of the incoming data. These requirements make them expensive, heavy, bulky, and very power-hungry, requiring large batteries that make the system ill-suited for remote field work and drone-based operations proposed here. Furthermore, the centre frequencies of these systems are often fixed, making it difficult or even impossible to adapt the GPR to the specific yet different needs of astrophysics and cryospheric research.

To understand frequency domain radar, let's consider the most common implementation, frequency modulated continuous wave (FMCW) radar. Instead of a short pulse, FMCW sends out a comparatively long-duration frequency modulated signal. Since transmission and reception are performed simultaneously on two separate antennas, it is described as a continuous wave. Instead of directly measuring the TOF of incoming reflections, this quantity is determined by comparing the frequency of the incoming signal to that being currently transmitted. In the case of the most widely used type of frequency modulation, linearly frequency modulated signal (LFM), otherwise known as a chirp, the range resolution of the system is determined by the swept bandwidth according to

$$\Delta R = \frac{c}{2B}. \tag{2}$$

Noting that in the case of the time-domain pulse radar, $B = 1/\tau$ [3], this is the same result as equation 1. Producing chirps is a much easier task than ultra-short pulses and can be done on readily available equipment, making these methods much more accessible for development than time domain radar.

1.3 Software-Defined Radio

Our GPR system will be powered by a software-defined radio (SDR). As the name suggests, SDRs make use of software to replace conventional analog devices such as mixers and filters, allowing us to produce, record, and perform signal processing on the board directly through software, providing a highly adaptable development platform [6]. SDRs consists of a small board with a field programmable gate array (FPGA) and a radio frequency (RF) front end. This flexibility not only enables rapid prototyping of different designs that would otherwise require costly custom circuit developement, but allows the GPR operating parameters to be tweaked and adapted for any requirement. For the purposes of this project, we've selected the Ettus B210 SDR. A proven platform, this board boasts 2x2 full duplex RF architecture which allows it to run a transmit channel as well as two receive channels, which is required for us to have a phase-coherent reference as well as the received signal. A high instantaneous bandwidth of 56MHz and wide tunable frequency range of 70MHz to 6GHz will also allow us to adapt the system to our evolving needs and different use-cases [7].

1.4 Matched Filters

The range profile of a signal consists of a plot of the reflected intensity over distance. Assuming that our received signal will consist of the reflection of our transmitted signal at various points and interfaces, we require a method of detecting those individual reflections. Detection
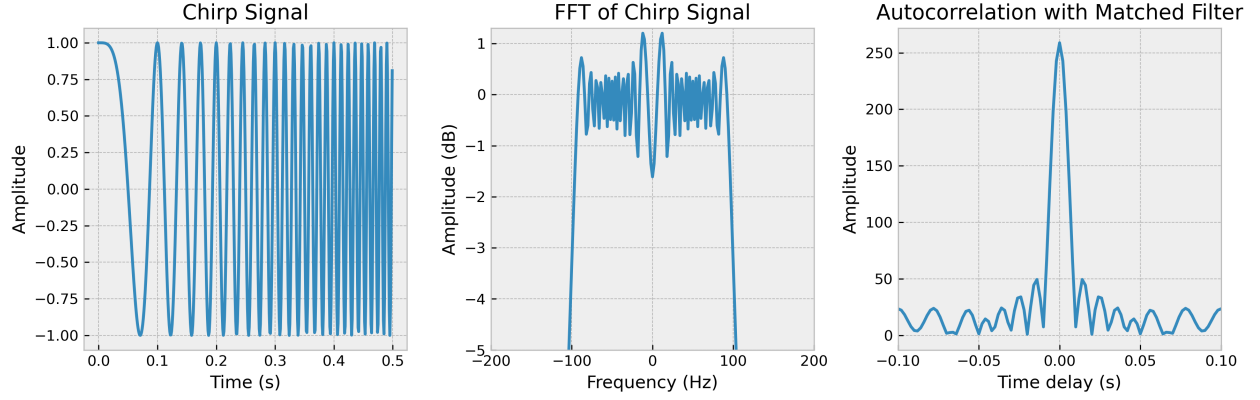
Figure 1: From left to right, a time domain plots of a chirp with parameters $T_p = 0.5$, $B = 100$ Hz, and $K = 200$, the Fourier transform of the chirp showing its rectangular frequency distribution, and an autocorrelated matched filter output.

can be achieved using a matched filter. It derives its name from its operating principle: A signal is convolved with a time-inversed reference signal, serving as the template waveform to detect. The resultant plot shows the degree to which the two signals "match" at every point. When autocorrelating a chirp using matched filtering, i.e. running the filter with two identical chirps, the output will be a sinc function centered at zero, as seen in Fig. 1. Since a time-domain convolution is simply a frequency domain multiplication, the matched filter can be processed in frequency space and is represented mathematically as

$$Y[\omega] = X[\omega] \cdot H[\omega]^*. \tag{3}$$

Here, $X[\omega]$ is the received signal, and $H[\omega]$ is the reference chirp, where $*$ specifies the complex conjugate of the signal. The matched filter is ideal for our use-case due to its simplicity and computational speed, but most importantly for its very low signal to noise ratio (SNR) [8].

1.5 Project Goals

Current commercial GPR systems typically employ wheeled carts or sleds for surveying operations. The land-based systems require manual surveying of the area of interest, which can be time-consuming and inaccurate. For glaciology surveys, these sleds must be dragged through the survey area by snowmobile, limiting accessible survey sites and adding logistical complexity. Moreover, commercial systems are heavy, expensive, and often closed-source and -hardware. The requirement for a custom-made, reliable, scalable, and autonomous soil mapping method led us to the development of a drone-based GPR system that uses off-the-shelf components, with an SDR and a synthetic wideband waveform (SWW) reconstruction algo-
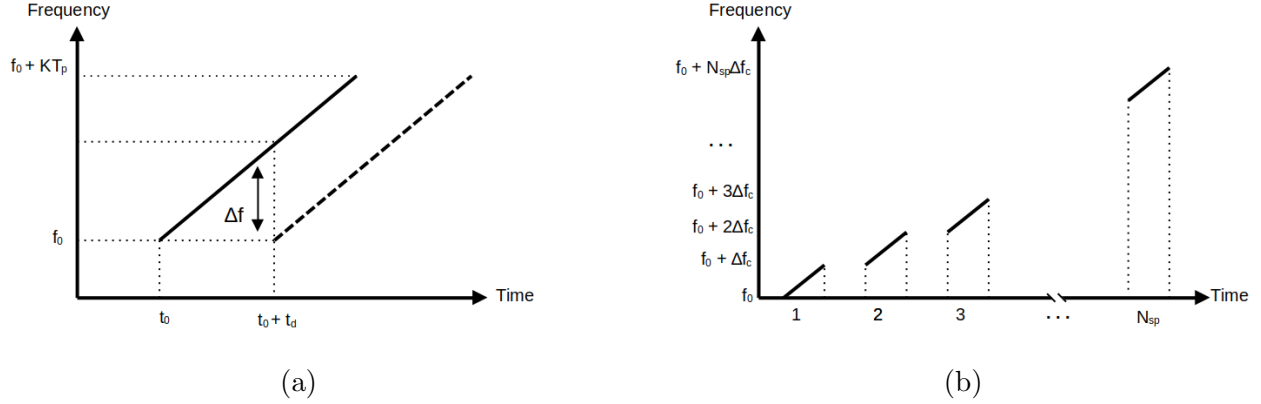
Figure 2: Illustrative graphs showing in (a) the time domain power spectrum of an LFM reference chirp in solid and a delayed chirp in dashed with the instantaneous frequency difference Δf, and in (b) the stepped frequency chirp signal.

rithm paired with FMCW as its backbone. The goal of the project is to develop the required tools to demonstrate the proof of concept application of GPR on an SDR and develop a first working prototype. This thesis outlines advances made to the system in both the SWW algorithm and the SDR scan script and presents results as well as describing the next steps to get the system ready for field use.

2 Synthetic Wideband Waveform Reconstruction

While FMCW is a well defined frequency domain radar method, numerous methods exist to implement the signal processing techniques required to create a range profile. We also require a way to artificially increase the bandwidth of our LFM chirp. The specific frequency stacking algorithm used to increase bandwidth, which we'll refer to as synthetic wideband waveform (SWW) reconstruction, is heavily inspired by work in [8] and [9]. In this section, we describe the fundamentals of FMCW radar, discuss the rationale behind utilizing matched filters, the significance of SWW in improving FMCW performance, and outline the frequency stacking algorithm.

2.1 Frequency Modulated Continuous Wave

As previously stated in section 1.2, FMCW radar is a common frequency domain radar technique. The signal that we have chosen to send is LFM chirp. LFMs allow us to sweep over the full available instantaneous bandwidth of the B210 and maximize the frequency coverage of our steps, enabling us to cover a larger frequency range more efficiently. The chirp is represented graphically, both in time and frequency by Fig. 1, and can be described

Variable	Description
fs	SDR sampling rate
B	Chirp bandwidth
K	Chirp slope
T_p	Chirp period
N_{sp}	Number of sub-pulses in SWW reconstruction
f_0	Start carrier frequency
Δf_c	Carrier frequency step

Table 1: Description of variables parameterizing both the LFM chirp and the stacking algorithm.

mathematically as

$$h(t) = A(t)e^{j2\pi(f_c+Kt/2)t}, \tag{4}$$

where $A(t)$ is the amplitude of the chirp, K is the chirp rate variable, and j is $-\sqrt{-1}$ to avoid confusion with the sample index i used later. Here, f_c describes the carrier frequency of our chirp. In practice, we observe a frequency dependence in $A(t)$, discussed later in section 3.4, but this variability will be ignored here. The K parameter is described by

$$K = \frac{B}{T_p}. \tag{5}$$

The quantity B is the bandwidth of the chirp and T_p is the duration of the chirp in seconds. We can model the received signal as a time-shifted signal

$$x(t) = e^{j2\pi(f_c+K/2(t-t_b))(t-t_b)}. \tag{6}$$

Here, t_b is the time delay between the transmitted and received signal. The time delay, which corresponds to the time-of-flight distance to the object, is related to the distance R of the object causing the reflection by

$$t_b = \frac{2R}{c}. \tag{7}$$

The beat frequency of two signals can be found by mixing the signal with its reference, in a process called down-chirping. The beat frequency of two frequencies is simply given by

$$F_b = \Delta f, \tag{8}$$

where Δf is the frequency difference between both signals. In the case of our chirp, this quantity can instead be expressed as

7

$$F_b = Kt_b. \tag{9}$$

This relationship shows that the round-trip time of the target is directly proportional to the beat frequency. Recalling the definition for K from equation 5, the equation can be rewritten as

$$F_b = \frac{B}{T_p}\frac{2R}{c}. \tag{10}$$

To identify the beat frequency in the mixed signal, we take the discrete Fourier transform (DFT). The frequency resolution of a DFT is given by [3]

$$\Delta f = \frac{1}{T_p}. \tag{11}$$

This equation therefore defines the resolution of beat frequencies we can detect, ΔF_b, as

$$\Delta F_b = \frac{1}{T_p} = \frac{B}{T_p}\frac{2\Delta R}{c}. \tag{12}$$

Isolating for ΔR and simplifying, we now obtain

$$\Delta R = \frac{c}{2B}. \tag{13}$$

The de-chirping method described above is the easiest and most intuitive way of producing range profiles from FMCW radar using an LFM chirp. However, as mentioned in section 1.4, the SNR of signal mixing is not ideal. The matched filter, as descried in section 1.4, has an excellent SNR compared to de-chirping [10], which is critical for GPR where absorption by the soil will weaken our signal, making it crucial that we minimize the noise of our output range profile. Recalling the matched filter equation in the frequency domain from equation 3, we can set

$$X[w] = FT\{x(t)\}, \tag{14}$$

and

$$H[w] = FT\{h(t)\}, \tag{15}$$

where FT denotes the Fourier transform. The output of the matched filter is given by

$$y_{out}(t) = FT^{-1}\{X[w] \cdot H[w]^*\}. \tag{16}$$

Ignoring the phase of the signal, the magnitude of the compressed signal after matched filtering is

$$|y_{out}(t)| = T_p|\text{sinc}[B(t - t_b)]|. \tag{17}$$

This result shows that the matched filter output will contain a sinc profile with the main peak centered at t_b. The range resolution of the matched filter is governed by the 4dB width of the sinc main lobe. Incidentally, the 4dB width is $1/B$, resulting in the same range resolution ΔR obtained in equation 13 with the de-chirping method. The maximum range is defined by a similar relationship to bandwidth, according to the equation

$$R_{max} = N_{sp}\Delta r = \frac{c}{2B}. \tag{18}$$

We can now completely describe the theoretical performance of an FMCW radar. While the instantaneous bandwidth of the B210 is cited as being 56 MHz, extensive testing carried out over the summer and fine-tuning data transfer parameters set an upper limit of 20MHz for the sampling rate, provided the board is receiving enough power. The maximum bandwidth we can send with a chirp signal at this sampling rate is 10MHz, a quantity governed by the Nyquist sampling theorem. Plugging this value into equation 13, we see that the range resolution of a chirp with this bandwidth is 15m. This is wholly insufficient for GPR applications, where we aim to measure features on the order of centimeters. To overcome this limitation, we can synthetically create large bandwidth chirps and increase the range resolution of our system.

2.2 Stepped FMCW

At its most fundamental level, stepped FMCW works by first sending out a chirp waveform at a given starting carrier frequency f_0. Once the chirp has been sent out, the local oscillator (LO) of the SDR is tuned to a new frequency, $f_0 + \Delta f_c$, and another chirp is transmitted. The LO is tuned again, the chirp is transmitted, and so on. This process is illustrated in Fig. 2 The ith chirp in the series is represented as

$$h(t) = A(t)e^{j2\pi(f_c+i\Delta f_c+Kt/2)t}. \tag{19}$$

To avoid gaps and overlaps between adjacent pulses in frequency space, we set $\Delta f_c = B$. This process is continued N_{sp} times until the desired bandwidth is swept. We can define the effective swept bandwidth, B_{eff} as

$$B_{eff} = N_{sp}B. \tag{20}$$

It is clear by analysis of equation 13 that the range resolution of our frequency domain radar is now described by [8]

$$\Delta r = \frac{c}{2B_{eff}}, \tag{21}$$

which clearly shows the advantage of implementing a stepped frequency algorithm. We can now achieve any desired range resolution despite the low 10MHz bandwidth of our chirps, B.

2.3 Reconstruction Algorithm

Once all the chirps have been transmitted and their reflections recorded, we have to stitch them together to produce a single, wide bandwidth signal. The process to accomplish frequency stacking using SWW reconstruction is described below:

1. Take the DFT of both the reference and transmitted chirp, which will produce a rectangle of width B as shown in Fig. 1

2. Upsample the DFT to the full bandwidth, B_{eff}, by sufficiently zero padding the single pulse DFT.

3. Perform a circular shift on the upsampled DFT to step the chirp spectrum up to the correct frequency. The frequency by which to shift the array is given by $i\Delta f_c$, where i is the pulse index.

4. Sum up the upsampled and shifted DFTs to produce one wide bandwidth signal, as seen in Fig. 3.

The reconstructed signal can then be used in the matched filter operation to produce a range profile, as described in section 2.1.

3 Communicating with the SDR

A primary challenge of our project was communication with the SDR. The B210 utilizes the USRP Hardware Driver (UHD)[1], a C++ API enabling waveform transmission, reception,
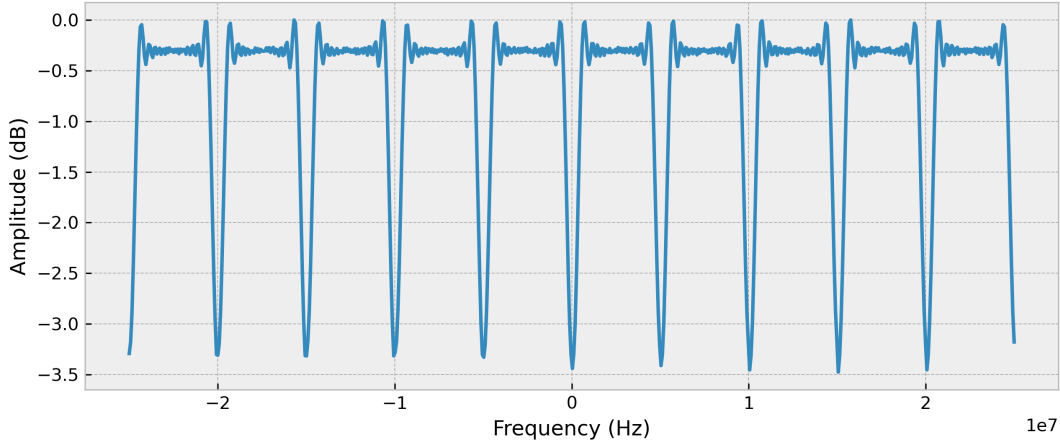
---

[1]https://www.ettus.com/sdr-software/uhd-usrp-hardware-driver/

Figure 3: Frequency stack output using the SWW algorithm with parameters $fs = 10$MHz, $B = 5$MHz, and $N_{sp} = 5$. Note that artificial noise was omitted for the sake of clarity.
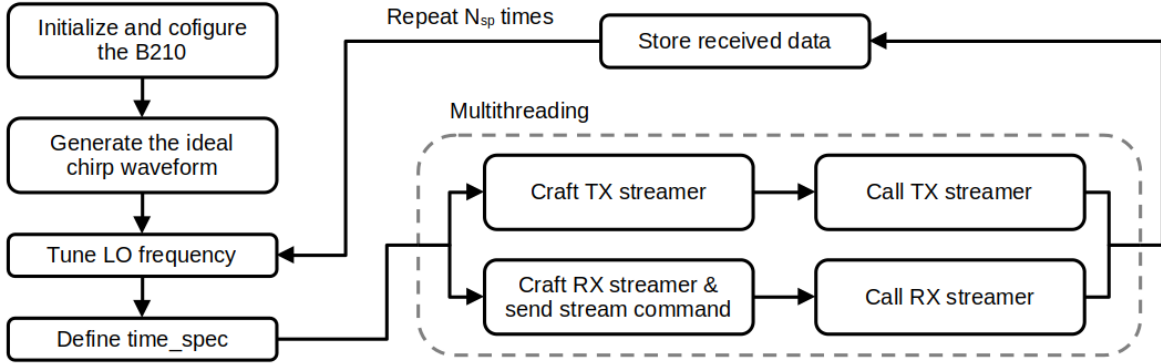

Figure 4: Process flow diagram describing the SDR communication and scan script

and control of parameters like sampling rate, center frequency, and gain. While GNURa-dio[2], an open-source diagrammatic toolkit, is commonly used with UHD, offering ease of SDR implementation, it lacked the necessary flexibility and fine-tuning capabilities for our GPR requirements. Consequently, we transitioned to the UHD Python API for enhanced control, although the lack of comprehensive documentation and example code made script development cumbersome. An initial script was developed and was later handed over to me to continue development. At this stage, the script was successfully communicating with the board but was unstable. The general structure of the script is described in Fig. 4, where the SDR has three main tasks: Configuring the board parameters, generating the chirp waveform, tuning the local oscillator, and simultaneously transmitting (TX) the chirp and

[2]https://www.gnuradio.org/

11

receiving (RX) the reflections, also known as transceiving. The task of transceiving the chirp is split into two workers, the TX Worker and the RX Worker, and are executed simultaneously using multithreading. This section will go over the these two workers, and discuss issues in the script that caused the instabilities and their fixes and final performance.

3.1 TX Worker

The TX worker is the simpler of the two tasks. In our system, there are two devices: The host computer running the script with UHD, and the SDR device, which is connected to the hots via USB-3.0 and is receiving commands from the host. Interfacing between the host and the SDR for transmission is the `tx_streamer` object, acting as the layer between samples on the host and samples on the SDR's transmit digital signal processor (DSP). The command to transmit is handled by calling `tx_streamer.send()`, which sends the chirp samples as well as accompanying metadata for the SDR. In the metadata, we can specify a transmit time, denoted `time_spec`. For a GPR scan, timing is crucial to ensure that you are receiving the full transmitted pulse without clipping, preserving all the information about reflections without loss.

3.2 RX Worker

Receiving data from the SDR is a bit more complex. Similarly to the transmission, we use the `rx_streamer`, although it only handles the incoming data. Without first instructing the SDR to begin reception, we will not receive any data. To inform the SDR, we use `stream_command`, which controls the RX DSP and defines how the device sends samples to the host. First, we set the mode parameter, which tells the SDR how to stream. For our purposes, we use `num_done`, or "num samps and done", where only a predefined quantity of samples will be received before ending streaming. The parameter `num_samps` defines the number of samples and is set to the length of our generated chirp, the same we are transmitting. For timing, we first set the `stream_now` attribute of the `sream_command`to False, before setting the `time_spec` value through the attribute of the same name. This timing condition ensures that once the stream command is sent, the SDR will begin reception at the same that transmission begins, ensuring our timing needs are met. Once the stream command is transmitted, we can call `rx_streamer_recv()`. Both the TX worker and RX worker are called in two separate threads thanks to multithreading. This technique allows both TX and RX operations to be set up side by side, which will allow the host to transmit samples to the SDR and receive the incoming samples, format them, and store them for later processing.

3.3 Fixes

While the script was functional, there was a big issue that prevented us from using the data and producing proper range profiles. The script ideally outputs a file containing the received samples over time, which when plotted, should show evenly spaced chirps, with some zero-padding between them. However, we noticed that the chirps were not only unevenly spaced but were also being clipped, as shown in Fig. 5a It was found that the cause of this behavior was the improper synchronization between our transmit and receive commands. While transmission was correctly respecting the `time_spec` wait condition, reception was not. As a result, our transmit and receive commands not lining up, resulting in clipped data. The reconstructed signal would therefore contain gaps, introducing large artifacts that made the resulting range profile unusable. The issue was caused by improper formatting of the `time_spec` value in the RX worker. Since our delay is defined in seconds, we were initially calling the current time with `usrpget_time_now()`, converting that to seconds using `get_real_secs()`, adding the delay, and passing that as the `time_spec` attribute, without converting back to the `time_spec` object. Moreover, the API did not provide any error to signal this syntactic error. To fix the issue, we instead converted the specified time delay into a `time_spec` object, added that to the current time (without conversion to seconds), and passed that to the `time_spec` attribute.

Following this fix, our pulses were coming in at the right time, and all the chirps were being fully recorded, as seen in Fig. 5. It is worth noting the difference in the shape between the chirp envelopes in Fig. 5a and Fig. 5b. The sharp spike observed in Fig. 5a is caused by a small DC offset at the start of the chirp, likely due to the quick ramp in frequency. This artifact appears to go away at higher sampling rates, as seen in 5b, but the envelope of the chirps now takes on a rounded shape, showing that $A(t)$ has some variability that has yet to be explained. More importantly, we notice that the amplitudes of the chirps is different at each carrier frequency, suggesting that there is some frequency dependence in the gain of the SDR. Similar behavior has been observed in other similar projects [8], and is generally corrected with the help of a lookup table. However, more extensive testing is required to fully understand the cause of the gain instability at the hardware level and to implement a robust corrective measure.

3.4 Performance

One major drawback of frequency domain radar, specifically implemented on an SDR with frequency stacking, is the duration required to perform a single A-scan. In the system's current configuration, a scan takes around 10 seconds, most of which is spent tuning the local
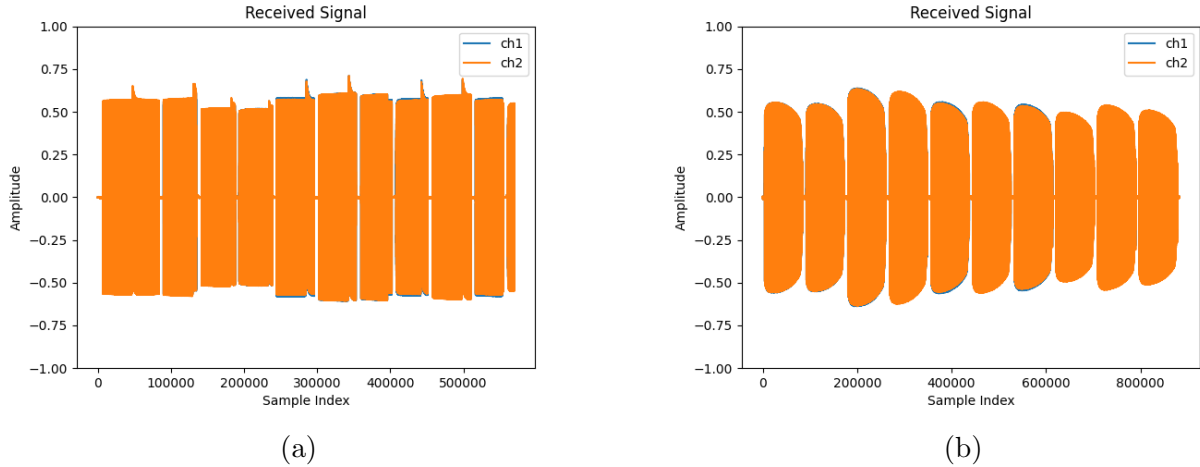
(a)   (b)

Figure 5: Received reference signal (ch1) and delay signal (ch2). Plot (a) has incorrect timing parameters, as seen by the overlap of chirp 1 and 2 and the last chirp being clipped. Transceiver timing was fixed in (b), as is evident by the even spacing. Sample rate f_s for plot (a) was set to 2MHz, whereas (b) was sst to 20MHz.

oscillator for each frequency step. Moreover, the maximum sampling rate of the system is currently limited to 20MHz before sample over- and under-flows occur, limiting the bandwidth of our signal to 10MHz. While we carried out extensive transfer parameter optimization, there is more work to be done in increasing data transmission rates.

4   Results

At this stage, we have a working SWW algorithm and can effectively communicate with the SDR with correct timing. The logical next step in the project was to test the GPR system in real-world scenarios and verify not only that we are able to produce high-quality data, but that we are able to generate sensible range profiles and achieve desired range resolutions greater than what is feasible with the limited instantaneous bandwidth of our SDR. This section outlines two such tests; the direct loopback configuration and the antenna wall reflection test.

4.1   Direct Loopback

For the first test, we sought to keep the conditions as simple and sterile as possible to provide a sanity check before introducing the antennas and all the noise and constraints that inevitably come with it. The direct loopback configuration was chosen and is illustrated in Fig. 7. As previously stated, we required a reference signal which will serve in our matched filter later.
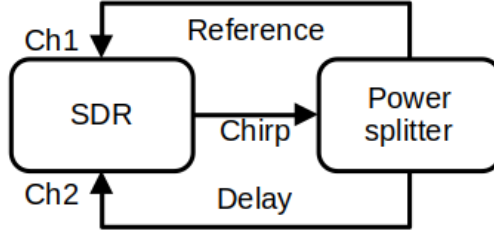
Figure 6: Loopback diagram

The transmitted signal is first routed through a cable into a power splitter, which evenly splits the incoming signal into two outputs. The first output was routed directly back into channel 1 of our SDR to serve as the reference signal. The second output was routed back into channel 2 of the SDR through a long cable. This cable, denoted the delay cable, will introduce a time delay into our received signal proportional to the length difference between the reference and delay cables. We should then be able to see a peak in our range profile corresponding to half this length difference, due to the factor of 1/2 in equation 7 which accounts for the round-trip of the signal. The value of c in the cables is governed by the velocity factor. For our setup, a velocity factor of 0.69 was used [11]. Chirp parameters were set to $f_s = 20$Mhz, $B = 10$Mhz, $f0 = 400Mhz$, $N_{sp} = 60$, for an an effective bandwidth of $B_{eff} = 600$Mhz. The range resolution is therefore $\Delta R = 10.5$cm

We first configured our loopback with equal-length reference and delay cables to verify that all parts were properly integrated and that we could detect a length of 0cm. Fig. 7a shows the range profile. As expected, we see a strong peak at the 0cm mark confirming the proper functioning of the system. It's worth noting the slight hump at the end of the range profile. This feature is the beginning of a second peak, which is a repetition of the first, due to R_{max} imposed by the FMCW method. We truncate our range profile at R_{max} distance. Next, introducing delays in the cable corresponding to distances of 15cm, 132cm, and 156cm, we see that the peak in our range profiles follows quite accurately. The matching is not perfect, due in partto our range resolution being relatively large, but mostly due to the uncertainty in the value of c throughout the setup including the power splitter [3]. Satisfied with these preliminary tests, it was time to move on to a more complex real-world test setup.
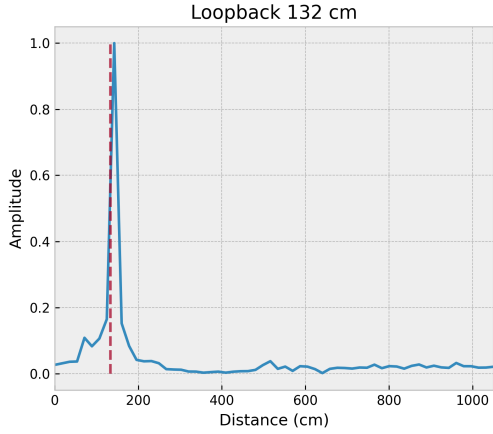
---

[3]In fact, if we were to use parameters that generate a very good ΔR, we could use regression analysis from the range profiles at known distances to determine with high precision the value for c in the loopback setup.
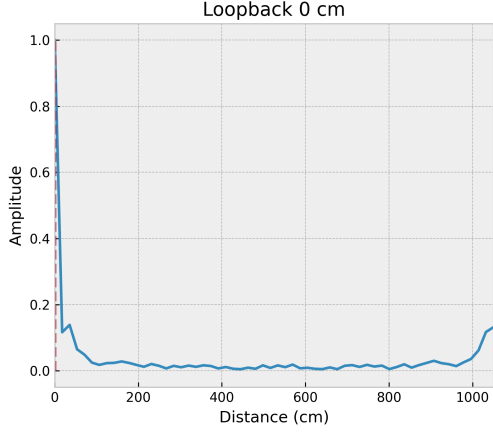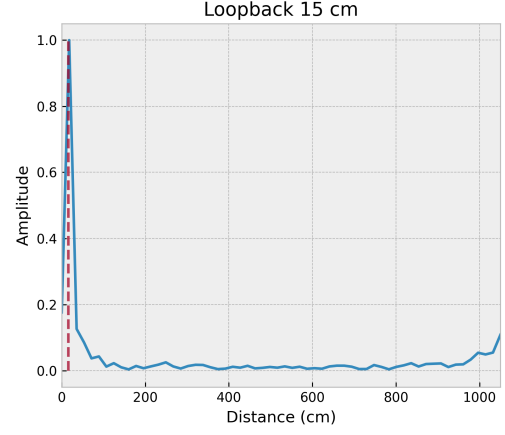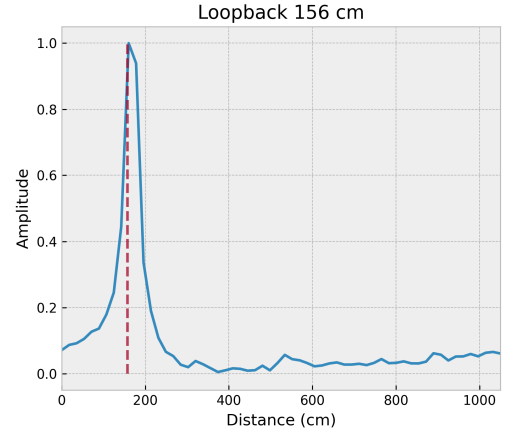
Figure 7: Range profiles for the direct loopback configuration, showing the full unambiguous range from 0cm to $R_{max} = 1050$cm. Predicted peak location of the induced delay distances of (a) 0cm, (b) 15cm, (c) 132cm, and (d) 156cm are indicated by the dashed red line. The peak corresponds to the measured distance using our GPR system.
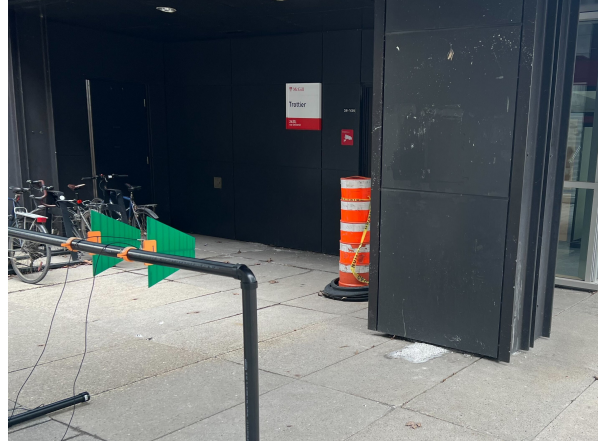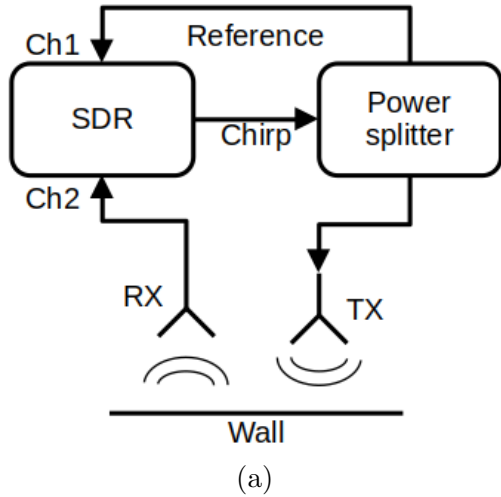
4.2 Wall reflection

Figure 8: Diagram (a) and image (b) of outdoor wall reflection testing with antennas directed towards metallic reflective surface.

The next series of tests is a closer representation of the setup for GPR operations. Instead of a long cable introducing a delay simulating an artificial target, we route one output of our power splitter into a TX antenna, and another RX antenna is then plugged into channel 2 of the SDR. As seen in Fig. 8b, antennas were then mounted to a frame constructed from plastic tubes at a set distance of 36.5cm apart. They were then aimed towards a large reflective surface; a metallic wall. This test aimed to introduce the antennas and propagation through air, while maintaining a very simple scan setup. Ideally, we will be able to resolve a single peak located at the distance between the antenna setup and the wall, assuming a near-perfect reflection off the metal surface. Here, we are assuming $c = c_0$, the speed of light in a vacuum. Using the same parameters are our direct loopback test, we have $\Delta R = 15$cm.

The results from our tests are compiled in Fig. 9, showing the range profiles at different distances. First, we notice the most prominent peak at the 0cm mark. Despite the high directivity of the log periodic antennas used in this setup [12], there is some crosstalk between them, which manifests as the largest peak due to their proximity. We use this peak to set the 0cm point in our range profile. Next, we see another large peak at the end of the plot. Like in the 0cm direct loopback plot, this peak is the repetition of the first crosstalk peak due to the R_{max} constraint, signaling the end of our unambiguous range. Finally, looking at Fig. 9a, we see a prominent peak at the 231cm mark, confirming the detection of the reflected pulse and the accurate measurement of the target. Fig. 9b shows a similar result at 343cm, though with a decrease in amplitude. At 448cm and 503cm, shown in Fig. 9c and Fig. 9d respectively, the peaks are still perceivable against the noise floor, but are visibly much fainter than at

closer distances. The spread of the transmitted beam means little power is made it back to the receiving antenna. We finally notice that the distances do not align perfectly at these larger distances, though this is due simply to the imprecise method of measurement chosen[4].

5 Conclusion

This thesis demonstrates the successful development of a functioning stepped FMCW GPR system, achieved through the implementation of a custom SWW algorithm and communication protocol with the SDR. We have reliably produced scans and generated range profiles both in a simple loopback setup and a reflective test. While these results mark a significant milestone in the project's progress, further steps and testing are required to prepare the system for GPR application.

5.1 Signal Amplification

Addressing signal strength issues is paramount. In air propagation, detection challenges emerged beyond the 3m mark, indicating potential limitations for GPR use due to soil attenuation and signal scattering. Calculating the necessary amplification using the radar equation will guide the addition of amplifiers to transmission and reception on the SDR, ensuring meaningful soil scans [3].

5.2 SWW & Scan Optimization

Although the GPR operates effectively, software enhancements are needed. The current SWW algorithm exhibits slow processing, hindering efficiency for tasks like B-scans. Improving processing speed and implementing signal reduction techniques are essential for maximizing scan quality. Additionally, optimizing scan duration to minimize errors introduced by drone motion is crucial. Exploring alternative reference signal approaches, such as utilizing generated chirp data, may enable hardware simplification for future drone integration.
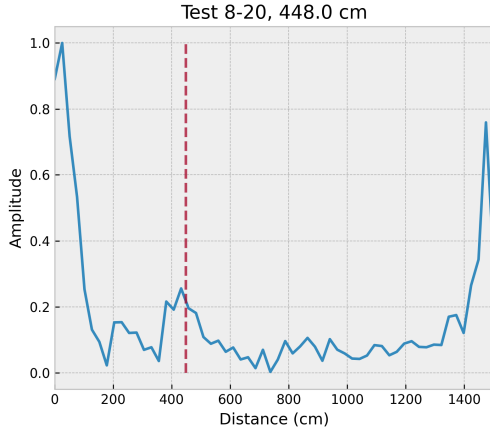

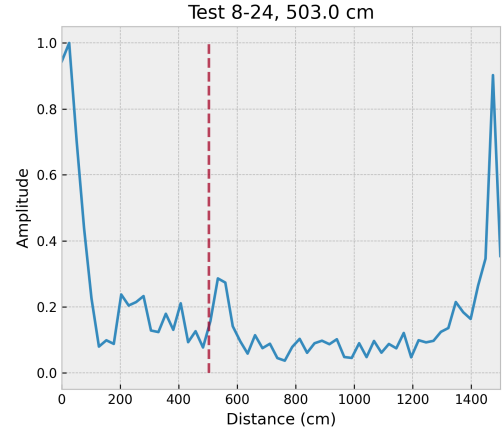
[4]Measuring tape is only so long!
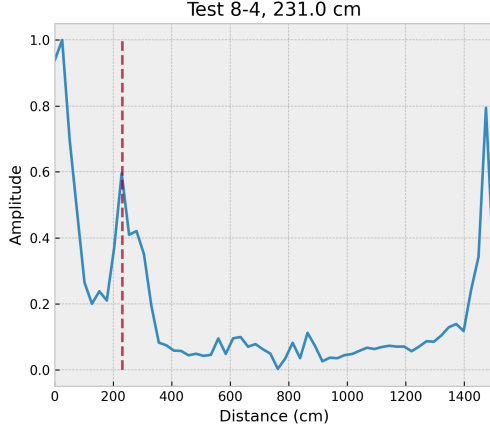
(a) $N_{sp} = 1$
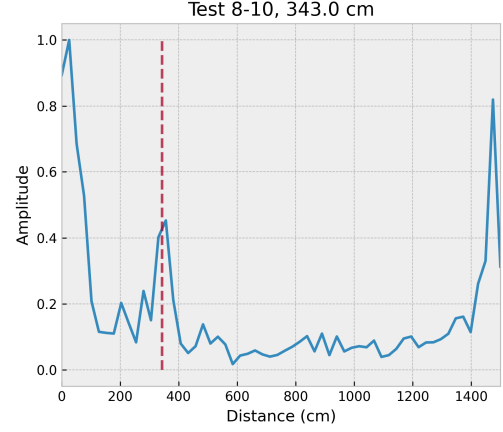
(b) $N_{sp} = 2$

(c) $N_{sp} = 10$

(d) $N_{sp} = 100$

Figure 9: Range profiles for reflective wall tests, showing the full unambiguous range from 0cm to $R_{max} = 1500$cm. Predicted peak locations corresponding to the reflection off the wall at distances of (a) 231cm, (b) 343cm, (c) 448cm, and (d) 503cm are indicated by the dashed red line. The first peak is the direct crosstalk between both antennas and the last peak is a repetition of this first peak. The third most prominent peaks are from the reflection off the wall. Note the noise floor.

References

[1] R. A. Monsalve, C. Altamirano, V. Bidula, R. Bustos, C. H. Bye, H. C. Chiang, M. Diaz, B. Fernandez, X. Guo, I. Hendricksen, E. Hornecker, F. Lucero, H. Mani, F. McGee, F. P. Mena, M. Pessoa, G. Prabhakar, O. Restrepo, J. L. Sievers, and N. Thyagarajan, "Mapper of the igm spin temperature (mist): instrument overview", (2023).

[2] M. Pessoa, "Development and testing of antenna and subsystems for mist, a 21-cm global signal experiment to study the cosmic dawn", MA thesis (McGill University, 2021).

[3] C. Ozdemir, *Inverse synthetic aperture radar imaging with MATLAB algorithms* (John Wiley & Sons, Mar. 2021).

[4] İ. Kaplanvural, K. Özkap, and E. Pekşen, "Influence of water content investigation on gpr wave attenuation for early age concrete in natural air-drying condition", Construction and Building Materials **297**, 123783 (2021).

[5] D. Picchi and S. Brell-Cokcan, "A modified common midpoint approach for GPR radars", Construction robotics **6**, 319–328 (2022).

[6] S. C. Carey and W. R. Scott, "Software defined radio for stepped-frequency, ground-penetrating radar", in 2017 ieee international geoscience and remote sensing symposium (igarss) (2017), pp. 4825–4828.

[7] *B200/b210/b200mini/b205mini - ettus knowledge base.*

[8] P. Fiske, "Software defined radio based frequency modulated continuous wave ground penetrating radar", PhD thesis (University of Vermont, 2020).

[9] S. Prager, T. Thrivikraman, M. S. Haynes, J. Stang, D. Hawkins, and M. Moghaddam, "Ultrawideband synthesis for high-range-resolution software-defined radar", IEEE Transactions on Instrumentation and Measurement **69**, 3789–3803 (2020).

[10] J. Wang, D. Cai, and Y. Wen, *Comparison of matched filter and dechirp processing used in linear frequency modulation*, 2011.

[11] *RG58 Coaxial Cable Specifications Sheet.*

[12] T. A. Milligan, *Modern antenna design* (John Wiley & Sons, July 2005).